ACS APPLIED MATERIALS & INTERFACES

Research Article

www.acsami.org

Surface Coating from Phosphonate Ionic Liquid Electrolyte for the Enhancement of the Tribological Performance of Magnesium Alloy

Ana Eva Jiménez,[†] Antonella Rossi,[‡,§] Marzia Fantauzzi,[§] Tulia Espinosa,[†] Joaquin Arias-Pardilla,[†] Ginés Martínez-Nicolás,[†] and María-Dolores Bermúdez*[,†]

[†]Departamento de Ingeniería de Materiales y Fabricación, Universidad Politécnica de Cartagena, 30202 Cartagena, Spain

[‡]Laboratory for Surface Science and Technology, Department of Materials, ETH Zürich, Switzerland, Vladimir-Prelog-Weg 5, CH-8093 Zürich, Switzerland

[§]Dipartimento di Scienze Chimiche e Geologiche, Cittadella Universitaria di Monserrato, Università degli Studi di Cagliari, I-09100 Cagliari, Italy

S *Supporting Information*

ABSTRACT: A chronoamperometric method has been applied for the growth of a surface coating on AZ31B magnesium alloy, using the imidazolium alkylphosphonate room-temperature ionic liquid 1-ethyl-3-methylimidazolium ethylphosphonate ([EMIM][$EtPO_3H$]) as electrolyte. A surface coating layer is obtained after 4 h under a constant voltage bias of −0.8 V with respect to the standard electrode. The coating nucleation and growth process correlates well with a 3D progressive mechanism. X-ray photoelectron spectrometry (XPS) analysis of [EMIM][$EtPO_3H$] shows new P 2p and O 1s peaks after its use as electrolyte, as a consequence of reaction between the phosphonate anion and the magnesium substrate. Angle-resolved XPS (ARXPS) analysis of [EMIM][$EtPO_3H$] did not show any change in the composition of the surface before and after chronoamperometry, since the sampling depth (1.5 nm at the highest emission angle) is larger than the cation and anion sizes (ca. 7 and 5 Å, respectively). Characterization of the coating was made by scanning electron microscopy (SEM), focussed ion beam SEM, energy dispersive X-ray spectroscopy, XPS, and ARXPS. FIB-SEM shows that the coating presents a mean thickness of 374 (±36) nm and contains magnesium and aluminum phosphates. Linear reciprocating tribological tests under variable load show that the presence of the coating can reduce friction coefficients of the coated AZ31B against steel up to 32% and wear rates up to 90%, with respect to the uncoated alloy.

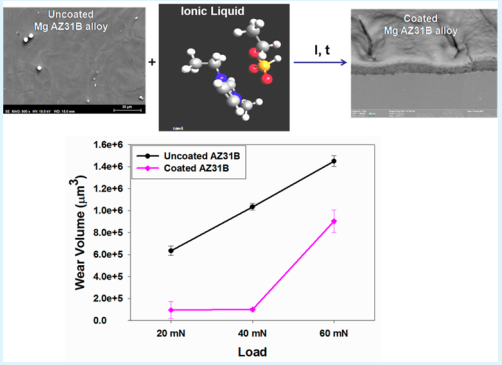

KEYWORDS: *phosphonate ionic liquids, coatings, chronoamperometry, reciprocating friction and wear, surface analysis, FIB-SEM, ARXPS*

1. INTRODUCTION

There is an increasing interest in the applications of magnesium alloys as structural materials in such demanding fields as transportation or electronics, as well as in prosthesis and implants due to their biocompatibility.[1,2] This is due to their high specific mechanical properties, high thermal and electrical conductivity, and their ease of manufacturing by conventional processes. In particular, magnesium alloy AZ31 is being extensively used in structural engineering applications. Unlike other lightweight materials such as aluminum alloys, no passive surface films are formed on magnesium alloys, as magnesium oxide is not protective, and they present a very poor corrosion resistance and tribological performance.[3−5] Many efforts are dedicated to corrosion protection of magnesium alloys,[6] mainly by deposition of surface layers and coatings. In contrast, wear resistance enhancement has received comparatively limited attention.

Room temperature ionic liquids (ILs) are fluids composed of ions that are stable in the liquid state at room temperature. They present a variety of properties such as high thermal stability, wide electrochemical window, high conductivity, negligible volatility, and nonflammability, which make them useful in a growing number of applications, from solvents to thermal fluids. From the materials science and surface engineering points of view, ionic liquids have shown outstanding potential as lubricants and lubricant additives[7−18] including lubrication of light alloys,[19−27] nanophase modifiers,[28,29] electrolytes,[30,31] corrosion inhibitors,[32−43] or promoters of corrosion protective surface coatings.[44−46]

Phosphonate derivatives are environmentally friendly compounds widely used as scale inhibitors in water treatment and industrial applications.[47] Phosphorus-containing coatings, in particular phosphonate derivatives,[48−50] are currently being studied as corrosion protective layers on magnesium alloys due

Received: February 6, 2015
Accepted: April 23, 2015
Published: April 23, 2015

ACS Publications © 2015 American Chemical Society

DOI: 10.1021/acsami.5b01167
ACS Appl. Mater. Interfaces 2015, 7, 10337−10347

to their biocompatibility. Phosphorus-containing ionic liquids have been extensively applied in corrosion protection of magnesium alloys.[51−65] A major cause of surface failure of magnesium alloys is their poor tribological performance under both dry and lubricated conditions.

Alkylphosphonate imidazolium ionic liquids[66] have previously shown to be highly reactive toward copper.[67] We have very recently reported the formation of surface layers on AZ31B magnesium alloy by immersion in different imidazolium alkylphosphonate ILs during 168 h at room temperature.[68] The new coatings increase the abrasion resistance of the alloy under scratching. An attempt has been made to optimize the formation of protective coatings and reduce immersion times by increasing temperature to 50 °C.[69] In all cases, the coatings formed by immersion in [EMIM][$EtPO_3H$] presented the best tribological performance under scratching when compared with other alkylphosphonate alkylimidazolium ILs. The presence of other elements in the composition of magnesium alloys, such as Zn in EZ33A, prevents the formation of an abrasion protecting coating due to the low reactivity of Zn with ionic liquids.[68]

With these precedents, in the present work, we have selected the phosphonate imidazolium IL [EMIM][$EtPO_3H$] (Figure 1)

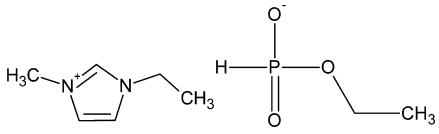

Figure 1. Chemical structure of [EMIM][$EtPO_3H$].

as precursor for the growth of surface films on the magnesium alloy AZ31B under electrochemical control, in order to improve its resistance to friction and wear in sliding under dry conditions.

2. EXPERIMENTAL SECTION

Imidazolium phosphonate ionic liquid [EMIM][$EtPO_3H$] (Figure 1) (purity >98%; electric conductivity 3600 mSm^{-1}; viscosity at 25 °C 0.07 Pa·s (standard deviation 7.5×10^{-4}), as determined with an AR-G2 rheometer (TA Instruments)) was commercially available from Solvionic (France) and used as received. Figure S1 (Supporting Information) shows the optimized geometry of the [EMIM][$EtPO_3H$] molecule calculated by molecular mechanics.

Magnesium alloy AZ31B (nominal composition in weight percentage: 3% Al, 1% Zn, 0.6% Mn, 0.1% Si, and Mg balance; hardness 57 HV) test coupons (25.5 mm diameter; 1.5 mm thickness) were polished to a mean surface roughness (R_a) of 0.08−0.09 μm, measured by a RT ALPA-SM contact profiler.

Chronoamperometry was carried out using an Autolab potentiostat (Metrohm) with a mini-cell of PTFE, using a three-electrode configuration, where the Mg sample acts as the working electrode, a rolled platinum wire is the counter-electrode, and a calomel mini-electrode (SCE) supplied by Bas, Inc., is the reference, with a potential of 0.242 V vs standard hydrogen electrode (SHE) at 25 °C. A 1:4.5 area ratio between the working and counter electrodes was used. The open circuit potential of the electrochemical cell stabilized at −1.90 V. The polarization curve is provided in Figure S2 (Supporting Information). Several voltage values corresponding to maximum current values were tested in order to determine the optimal values for the generation of the coating. In a chronoamperometry test, the voltage is maintained constant with time. The reaction between the magnesium alloy surface and the ionic liquid can be detected by a sharp increase of the current. In our system, this increment takes place at a voltage bias of −0.8 V vs SCE. The optimum time has been established to be 4 h (Table S1 and Figure S3, Supporting Information).

The coatings formed on the alloy were characterized by focused ion beam and scanning electron microscopy (FIB-SEM), energy-dispersive X-ray spectroscopy (EDX), and X-ray photoelectron spectroscopy (XPS). XPS analyses were performed using a VG Theta Probe (Thermo Fisher Scientific, East Grinstead, U.K.) spectrometer equipped with a monochromatic Al Kα source with a beam size varying between 15 and 400 μm, a pass energy of 100 eV, and an energy step of 0.05 eV. The characterization of the neat ionic liquid was also performed using a beam (200 μm diameter). All XPS binding energies were corrected using the hydrocarbon C 1s peak (285 eV). The accuracy of the binding energy measurements is of 0.2 eV. The uncertainty for the atomic percentages is ±10%.

To resolve peaks with very close binding energy values, after background subtraction,[70,71] we fitted the spectra using CASAXPS software (v.2.3.15, Casa Software, Ltd., Wilmslow, Cheshire, U.K.).

The tribological performance of the samples was tested using a CSM Nanotribometer NTR2, operating in linear reciprocating mode (ASTM G133-05 standard). The tests were carried out in the absence of lubricant under variable loads of 20, 40, and 60 mN with a 3 mm length at a speed of 5 mm/s and a total sliding distance of 3.6 m using AISI 52100 steel balls (2 mm sphere radius) as counterpart (35−45% HR; 25 (±1) °C). The wear volume was measured using a Sensofar PLu neox 3D optical profiler in confocal mode. Before surface analysis, samples from tribological tests were cleaned with dry ethanol and dried with nitrogen.

3. RESULTS AND DISCUSSION

3.1. Chronoamperometry. Table S1 and Figure S3 (Supporting Information) show the chronoamperometric curves at −0.8 V recorded at 1 and 4 h tests. The results are normalized to the maximum intensity and time in order to compare the curve with the electrochemical models of layer formation. The $I-t$ curves have a maximum after about 1000 s. Nevertheless, there are some deviations in the values and curve shapes, probably due to the heterogeneity of the samples and the temperature variations.

Previous studies[72,73] have established current−time relationships for determining both the kinetics of the nucleation mechanism and the growth process.

In instantaneous nucleation, the nucleation simultaneously occurs at a small number of active sites and presents a slow growth. In progressive nucleation, there are many active sites, the nuclei have a fast growth rate, and new nuclei are continuously formed. In this later case, the geometry of the growing particles is estimated from the assumption that either two-dimensional (2D) islands or three-dimensional (3D) clusters are formed.

The models for the different types of nucleation and growth mechanisms are given by the following equations:

2D instantaneous

$$\frac{I}{I_{max}} = \frac{t}{t_{max}} \exp\left[-\frac{1}{2}\left(\frac{t^2 - t_{max}^2}{t_{max}^2}\right)\right] \quad (1)$$

2D progressive

$$\frac{I}{I_{max}} = \left(\frac{t}{t_{max}}\right)^2 \exp\left[-\frac{2}{3}\left(\frac{t^3 - t_{max}^3}{t_{max}^3}\right)\right] \quad (2)$$

3D instantaneous

$$\left(\frac{I}{I_{max}}\right)^2 = \frac{3.8181}{t/t_{max}}\left\{1 - \exp\left[-1.2564\left(\frac{t}{t_{max}}\right)\right]\right\}^2 \quad (3)$$

DOI: 10.1021/acsami.5b01167
ACS Appl. Mater. Interfaces 2015, 7, 10337−10347

3D progressive

$$\left(\frac{I}{I_{max}}\right)^2 = \frac{1.2254}{t/t_{max}}\left\{1 - \exp\left[-2.3367\left(\frac{t}{t_{max}}\right)\right]\right\}^2 \quad (4)$$

where I_{max} and t_{max} are the current and time values of the maximum peak, respectively.

With the aim of characterizing the electrodeposition process, we analyzed the experimental values for [EMIM][$EtPO_3H$]. The experimental curve after 4 h of polarization together with curves calculated assuming 3D nucleation and growth mechanisms are provided in Figure 2.

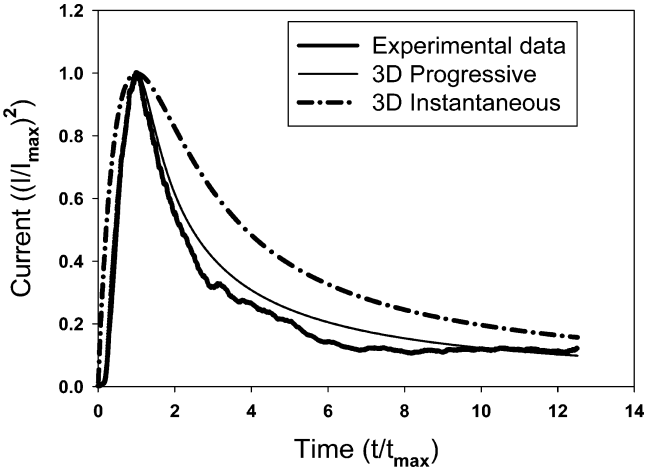

Figure 2. Chronoamperometry experimental results compared with theoretical 3D models.

The experimental curve is in agreement with a 3D progressive nucleation mechanism, particularly from the beginning up to $2t_{max}$. For longer times, a less accurate fitting is obtained, likely due to coalescence of the nuclei. It might thus be assumed that the coating particles are spherical and distributed throughout the entire electrode surface, with a rather broad particle size distribution. Figure S4 (Supporting Information) shows that the experimental curve is not in good agreement with a 2D mechanism.

3.2. FIB-SEM Study of the Coating Layer. The original AZ31B magnesium alloy SEM microstructure and EDX spectra are shown in Figure S45 (Supporting Information). Figure 3 shows a SEM micrograph and the EDX spectrum of the coating layer generated on AZ31B after chronoamperometry in [EMIM][$EtPO_3H$], showing the presence of a layer where phosphorus and oxygen from the phosphonate anion are present.

FIB-SEM was employed to characterize the coating layer thickness and the coating-substrate interface. Figures 4 and 5 show that the coating forms a uniform layer with a mean coating thickness of 374 (±36) nm, well adhered to the substrate, even on the intermetallic particles present in the AZ31B matrix (Figure 4). The EDX line analysis (Figure 5b) along the cross section shows a continuous decrease of magnesium concentration, together with increases of the oxygen and phosphorus concentrations from the substrate to the outer layer of the coating. An intermediate layer can be observed (Figure 5a), which confirms the good coating-substrate adhesion.[74]

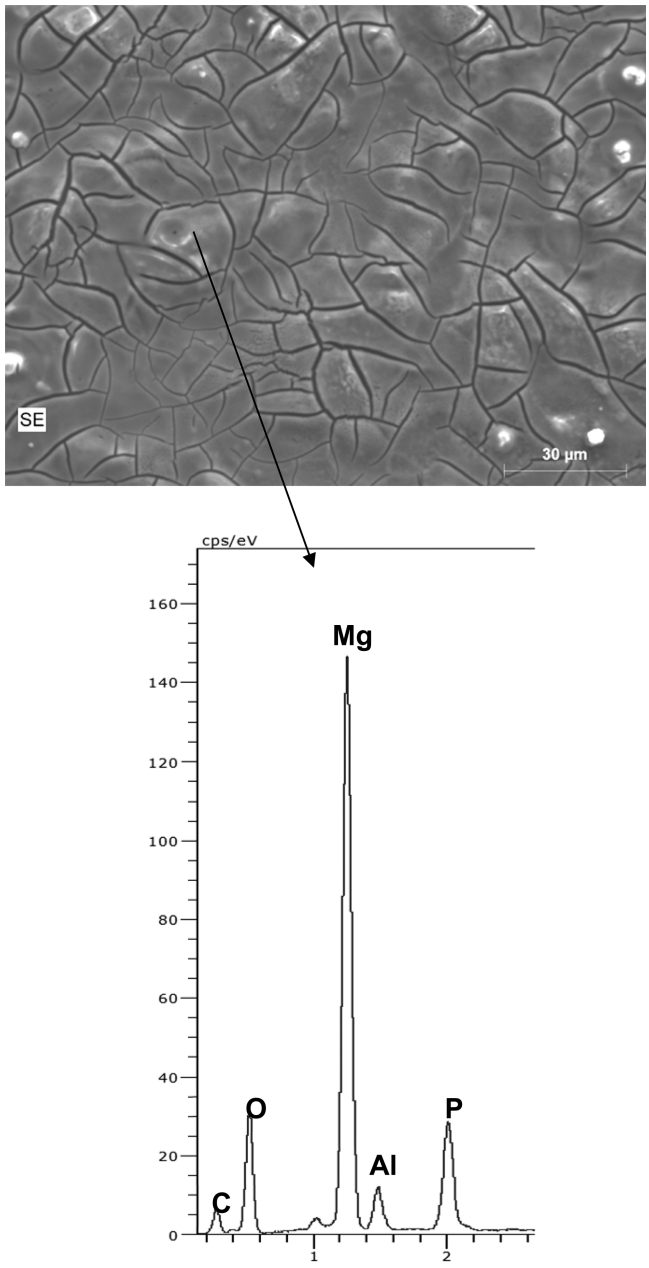

Figure 3. (Top) SEM micrograph and (bottom) EDX spectrum of the coating layer on AZ31B.

3.3. Tribological Tests. Figure 6 compares the friction-sliding distance records for AZ31B magnesium alloy and for the alloy coated with the layer electrochemically generated from [EMIM][$EtPO_3H$], under increasing normal load.

The initial friction value around 0.6 is similar in both cases during the first meter for both materials samples (coated and uncoated), independently of normal load (Figure 6a–c). Moreover, AZ31B alloy maintains similar friction values for all normal loads and sliding distances. Mean friction values for AZ31B (Figure 7a) show a slight decrease in friction as load increases from 0.60 under 20 mN to 0.53 under 60 mN.

Under lower applied loads (20 and 40 mN) the coated material shows a friction coefficient decrease after sliding 1 m and reaches mean friction values around or below 0.4 (Figure 6a) with a reduction of 28% with respect to the uncoated alloy under 20 mN and 33% under 40 mN. In contrast, under 60

DOI: 10.1021/acsami.5b01167
ACS Appl. Mater. Interfaces 2015, 7, 10337–10347

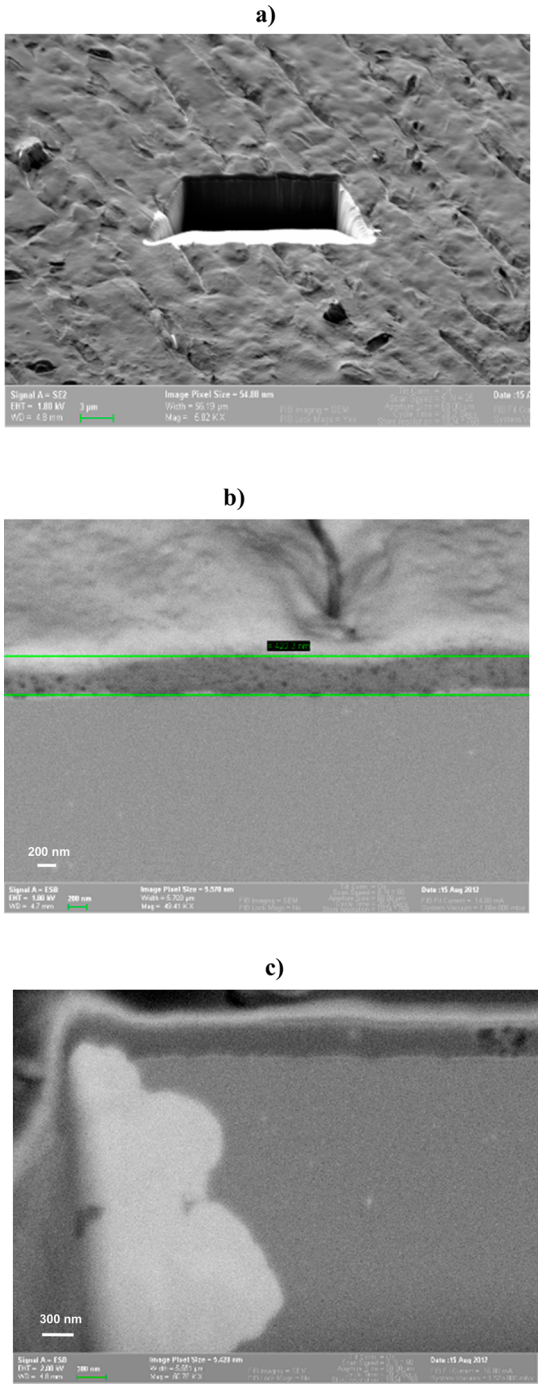

Figure 4. (a) FIB-SEM milling section; (b) magnification showing the cross section substrate-coating interface and coating thickness; and (c) detail showing the coating layer over an intermetallic precipitate particle (light gray).

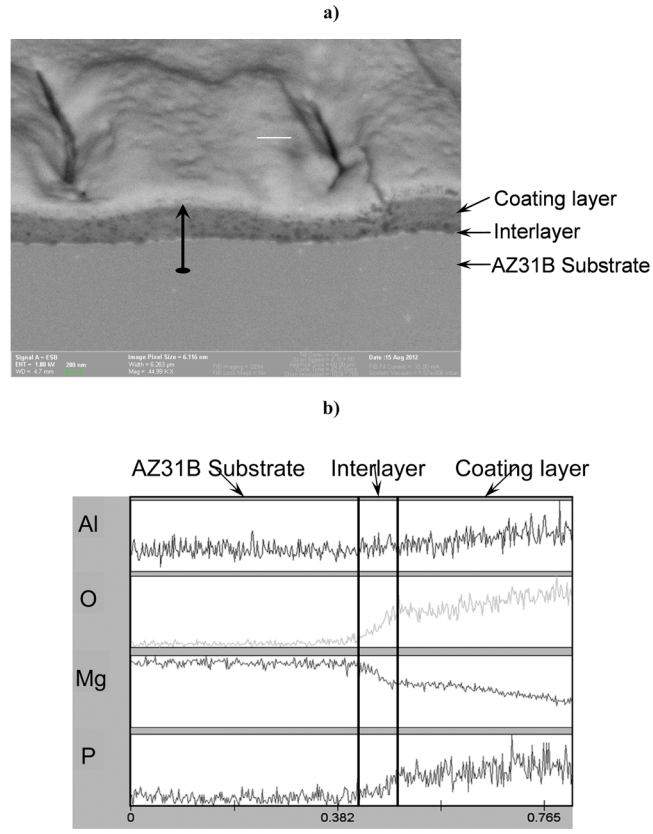

Figure 5. (a) FIB-SEM cross section indicating the different layers and the direction of element analysis shown in panel b; (b) element analysis along the cross section shown in panel a.

mN, the coated material presents a mean friction coefficient value slightly higher than the uncoated AZ31B alloy, showing the failure of the coating to protect the substrate under high contact pressures.

The high running-in friction period could be related to the compositional changes inside the wear path with respect to the original surface and, in particular, to the removal of magnesium oxide, as it will be discussed in section 3.4.

The uncoated alloy shows the expected wear dependence with load, with a linear wear volume increase under increasing load (Figure 7b), from 6.4×10^6 μm^3 under 20 mN to a maximum 1.5×10^6 μm^3 under 60 mN.

As observed for the friction coefficients, under lower applied loads, the coated material presents a milder wear volume of 1.0×10^5 μm^3, both under 20 and 40 mN. Therefore, the maximum wear reduction is obtained under 40 mN, with a decrease of 1 order of magnitude with respect to the uncoated alloy. A transition to more severe wear, to reach a wear volume of 8.9×10^5 μm^3 takes place when the load is increased to 60 mN (Figure 7b).

Figure 8 shows the wear scars on both materials as a function of load. Uncoated AZ13B magnesium alloy suffers extensive material removal as seen for the wear debris accumulated mainly outside both scar tips. In contrast, the coated material shows no wear debris formation under 20 and 40 mN.

Figure 9 compares the topography (Figure 9a) and cross section profiles (Figure 9b) of the wear scars under 40 mN for the uncoated AZ31B alloy and for the coated material covered with the layer generated from the phosphonate ionic liquid.

We have previously described[58,59] the abrasion mechanisms under scratching for AZ31B and for AZ31B covered with the coating layer generated by immersion in [EMIM][$EtPO_3H$] at room temperature, where the coating layer penetrates into the magnesium matrix along the wear path, by the action of the contact pressure.

3.4. X-ray Photoelectron Spectroscopy. Table 1 and Figure 10 show the binding energies and atomic percentages determined by XPS analysis for neat [EMIM][$EtPO_3H$] before and after chronoamperometry.

DOI: 10.1021/acsami.5b01167
ACS Appl. Mater. Interfaces 2015, 7, 10337−10347

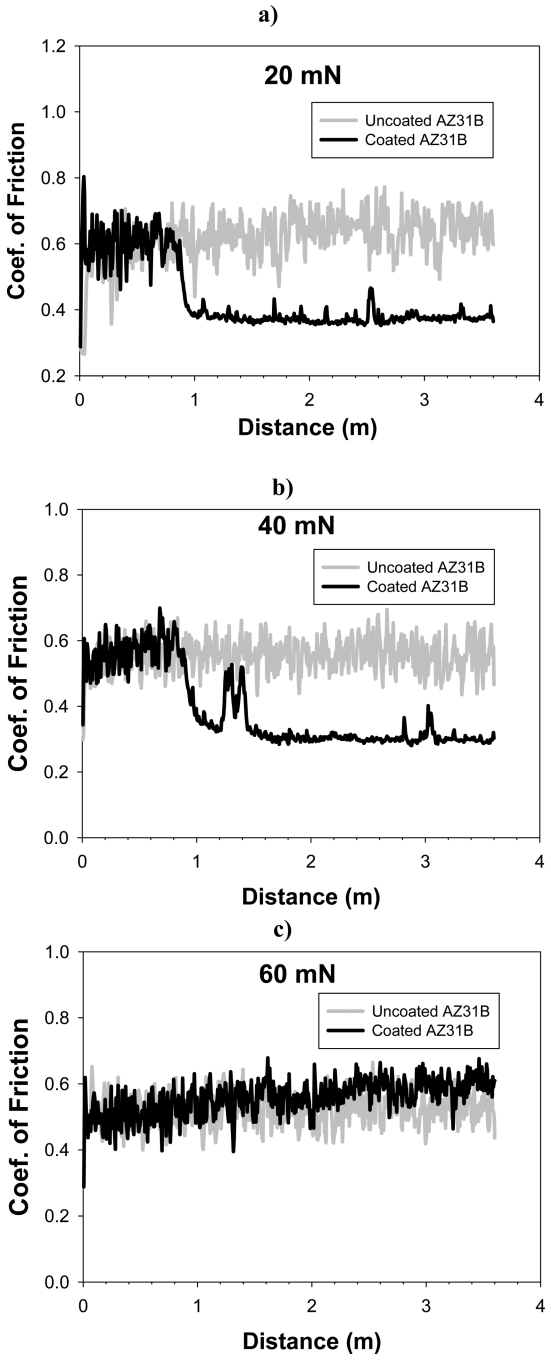

Figure 6. Friction coefficients vs sliding distance: (a) 20 mN, (b) 40 mN, and (c) 60 mN.

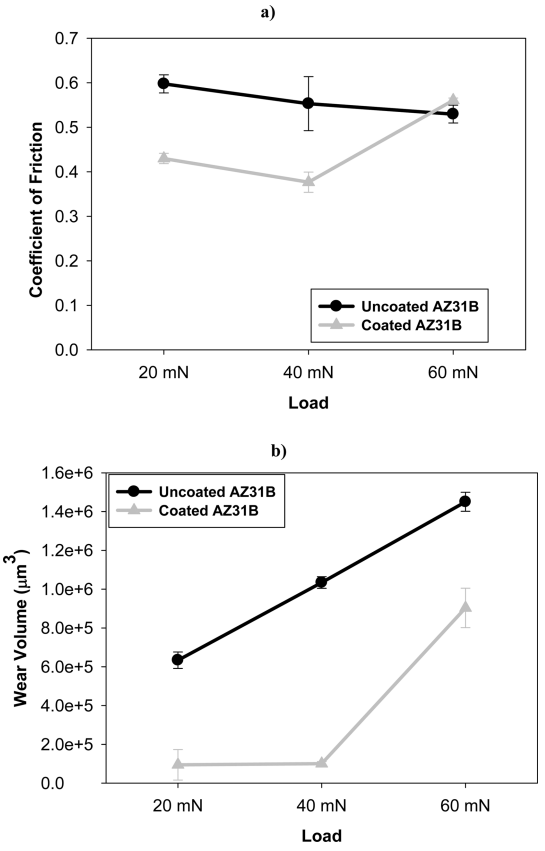

Figure 7. a) Friction coefficient vs normal applied load. b) Wear rates vs normal applied load.

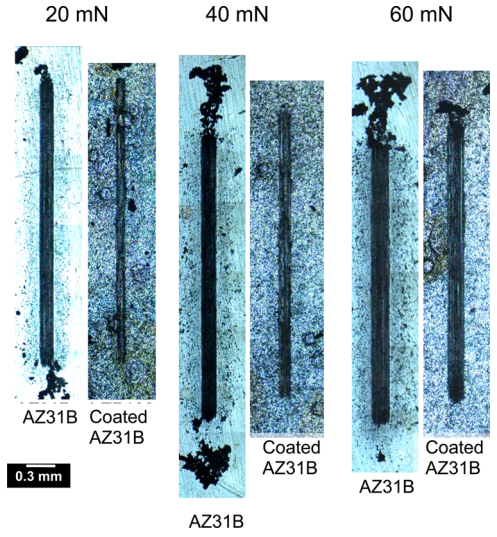

Figure 8. Comparative confocal microscopy images of the wear tracks on coated and uncoated AZ31B magnesium alloy, as a function of normal load.

The C 1s region is composed of four components due to the presence of four nonequivalent carbon atoms in the molecule (see Figure 1). The peak labeled C_1 (Figure 10a), whose binding energy was constrained at 285.0 eV, is due to alkyl carbon atoms in the IL. The peak at 286.1 eV, labeled C_2, is assigned to carbon atoms bound to oxygen and to nitrogen atoms of the imidazolium ring. The area of this component was fixed, and it was 1.5 times the area of C_1. The C_3 peak is due to the two carbon atoms $-N^+-C{=}C-N-$ in the imidazolium ring; the binding energy of this component is 286.4 eV, and the C_3/C_1 area ratio was constrained to 1. Finally, the fourth component C_4 is due to the carbon atom bound to two nitrogen atoms in the imidazolium ring $-N^+{=}C-N-$. Its binding energy was 286.9 eV, and its area was half the area of the C_1 component.

The O 1s signal (Figure 10b) showed the presence of two different components at 530.2 and 532.2 eV with an area ratio of 2:1 due to the two $O{=}P-O^-$ oxygen atoms and the CH_3-CH_2-O-P oxygen atom, respectively. A third component at 532.9 eV is also present and it might be due to absorbed water.

DOI: 10.1021/acsami.5b01167
ACS Appl. Mater. Interfaces 2015, 7, 10337−10347

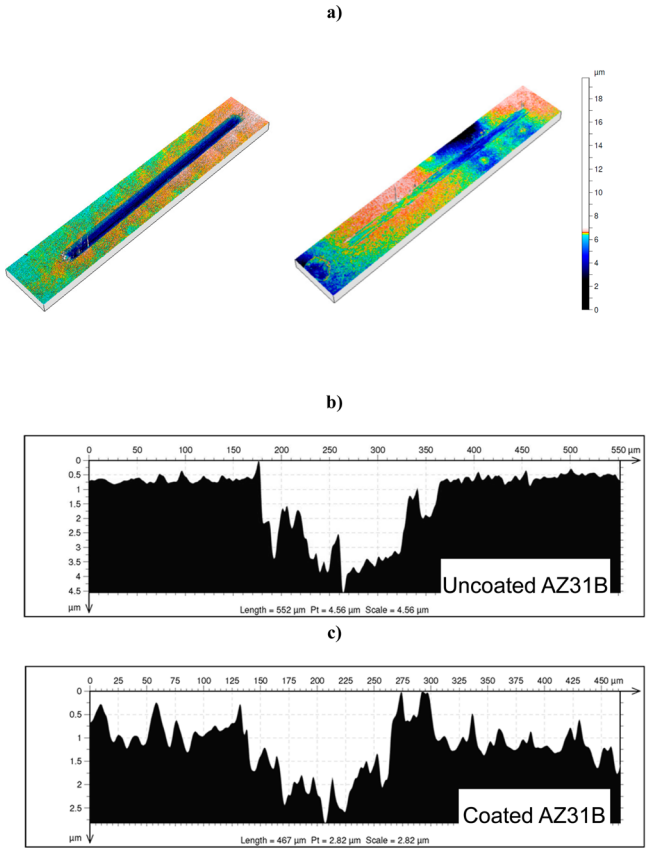

Figure 9. (a) Wear scar topographic profiles and (b and c) wear scar cross section profiles after the tests under 40 mN.

Table 1. XPS Binding Energy of the Elements Constituting [EMIM][EtPO$_3$H] before and after the Chronoamperometry Test

		XPS results of the pure ionic liquid		XPS results of remaining ionic liquid after chronoamperometry	
ionic liquid stoichiometry atomic %	element	binding energy (eV)	atomic %	binding energy (eV)	atomic %
57	C 1s	285.0	56	285.0	55
		286.1		286.1	
		286.4		286.4	
		286.9		286.9	
14	N 1s	401.6	13	401.6	12
7	P 2p	132.1	10	132.2	8
				133.1	2
21	O 1s	530.2	13	530.2	11
		532.2	7	531.0	3
				532.1	5
	O 1s (water)	532.9	1	532.8	3

The N 1s (Figure 10c) was centered at 401.6 eV while the most intense signal of phosphorus (Figure 10d), P 2p consists of a doublet due to the spin−orbit coupling, P 2p$_{3/2}$ and P 2p$_{1/2}$, separated by 0.9 eV and with an area ratio of 2:1.[75] The binding energy value of P 2p$_{3/2}$ component was found to be 132.1 eV.

Very good agreement between stoichiometry and experimentally determined composition of the pure ionic liquid was found (Table 1) except for phosphorus, which is higher (measured 10%) than the expected value (calculated 7%).

The XPS analysis was also repeated after chronoamperometry: the C 1s and N 1s signals did not show changes as far as shape of signal and binding energy values is concerned, whereas the O 1s and P 2p signals showed the presence of new peaks. The additional component of the O 1s signal is centered at 531.0 eV, while the binding energy of the second P 2p$_{3/2}$ peak is found to be 133.1 ± 0.2 eV. These two signals might be due to the presence of HPO_4^{2-} species.[76]

Angle-resolved XPS (ARXPS) was also used for checking the uniform distribution of the ionic liquid as a function of depth.[77] For organic samples, the depth probed for 0° is only of the order of 7−9 nm. Surface sensitivity can be increased by increasing the angle from 0° to greater than 70°. It is estimated that 80°, the depth probed is around 1−1.5 nm.[78]

Previous ARXPS[77] studies have shown a higher proportion of alkyl chains in the near surface region for nonfunctionalized ILs. In the present case, ARXPS of [EMIM][EtPO$_3$H] after its use as electrolyte (Figure S6a, Supporting Information) provides evidence that there is no gradient in the elemental distribution. The sampling depth (1.5 nm at the highest emission angle) is larger than the cation and anion sizes (ca. 7 and 5 Å, respectively).

The XPS analysis of the AZ31B magnesium alloy substrate before electrochemical treatment was determined as a function of sputtering time (Figures S7 and S8, Supporting Information). Figure S7 (Supporting Information) shows the evolution of the Mg 2p binding energy from 52.2 eV before sputtering to 49.4 eV after 2940 s of sputtering time.

In the same way, Figure S8 (Supporting Information) shows the evolution of O 1s peaks for AZ31B, from 534.6 eV before sputtering to 530.8 eV after sputtering. After 1440 s, the high binding energy peak disappears and the lower energy peak progressively decreases its intensity, in agreement with the observations for Mg 2p, as will be discussed below.

The high reactivity of magnesium alloys in air results in the formation of a reaction layer which contains magnesium compounds such as magnesium oxide, hydroxide, and carbonate.[79] To obtain a reference for the assignation of the Mg 2p and O 1s peaks, we analyzed commercial magnesium oxide, magnesium hydroxide, and magnesium carbonate by XPS (Table 2).

The binding energy values and the composition of the surface of the alloy are reported in Table 3. Mg is mainly present as hydroxide and carbonate, as confirmed by Mg 2p and O1 binding energies. Very small amounts of aluminum and zinc are detected.

Using these results as a reference, we assigned the AZ31B sputtering analysis described above (Figures S7 and S8, Supporting Information) to the initial presence of magnesium carbonate at the outer surface (low sputtering time), the presence of magnesium oxide, or hydroxide in intermediate depths, to reach finally the magnesium metal. However, the signal assigned to oxidized magnesium is present even after 2940 s.

The XPS survey spectrum of the coating after chronoamperometry shows the presence of Mg, Al, O, C, and P. A small fluorine contamination, probably from the PTFE electrochemical cell, was also detected.

Figure 11 shows the high-resolution Mg 2p, O 1s and P 2p spectra, after background subtraction and curve fitting, for the pure AZ31B magnesium alloy and for the AZ31B alloy covered

DOI: 10.1021/acsami.5b01167
ACS Appl. Mater. Interfaces 2015, 7, 10337−10347

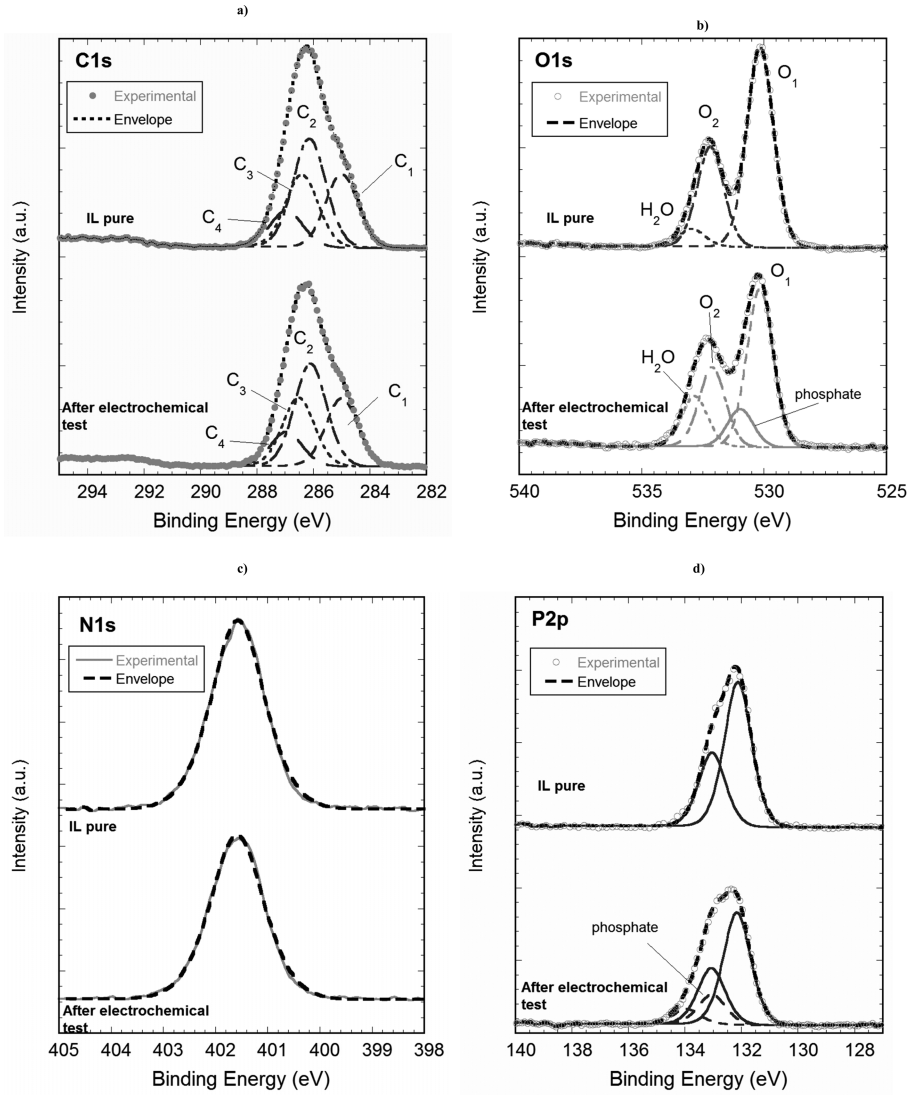

Figure 10. XPS analysis of the ionic liquid [EMIM][$EtPO_3H$] before and after the electrochemical process to generate the coating layer on AZ31B: (a) C 1s, (b) O 1s, (c) N 1s, and (d) P 2p.

Table 2. XPS Binding Energies (eV ± 0.2) of Magnesium Compounds[a]

	MgO	$Mg(OH)_2$	$MgCO_3$
Mg 2p	49.9	50.0	51.4
O 1s	530.1	531.5	531.8
C 1s			290.1

[a]Analyzed under the same conditions adopted for investigating the ionic liquid and the alloy before and after the chronoamperometry measurements.

Table 3. XPS Binding Energies and Atomic Percentages of Pure AZ31B and the Layer on AZ31B after Electrochemical Treatment in [EMIM][$EtPO_3H$]

	pure AZ31B		layer	
element	binding energy (eV)	atomic %	binding energy (eV)	atomic %
C 1s (carbonate)	289.7	5.0	289.9	3.5
Mg 2p	50.0	30.0	50.3	33.0
	51.0	8.0		
O 1s	531.2	34.0	530.1	3.0
	532.1	18.0	531.8	36.0
	533.3	4.0	532.6	15.0
Al 2p	74.2	0.4	74.4	5.0
Zn 2p	1022.0	0.5	1022.0	0.1
P 2p	n.d.[a]		133.0	3.0
	n.d.[a]		133.9	2.5

[a]n.d. = not detected.

with the coating layer generated in [EMIM][$EtPO_3H$], after chronoamperometry.

Following the chronoamperometry, the Mg 2p spectrum has only one component centered at 50.3 ± 0.2 eV and the oxygen signal has three components at 530.1 ± 0.2, 531.8 ± 0.2, and 532.6 ± 0.2 eV (Table 3). The phosphorus signal is also multicomponent with a doublet at 133.0 ± 0.2 eV and a second at 133.9 ± 0.2 eV. Table 3 also provides the elemental composition in atomic percentages: it might be stated that the coating layer is enriched in aluminum in comparison with the bulk composition and with the native oxide layer. Furthermore, based on the binding energy values, it is possible to assess that under these conditions the coating is mostly made of

DOI: 10.1021/acsami.5b01167
ACS Appl. Mater. Interfaces 2015, 7, 10337−10347

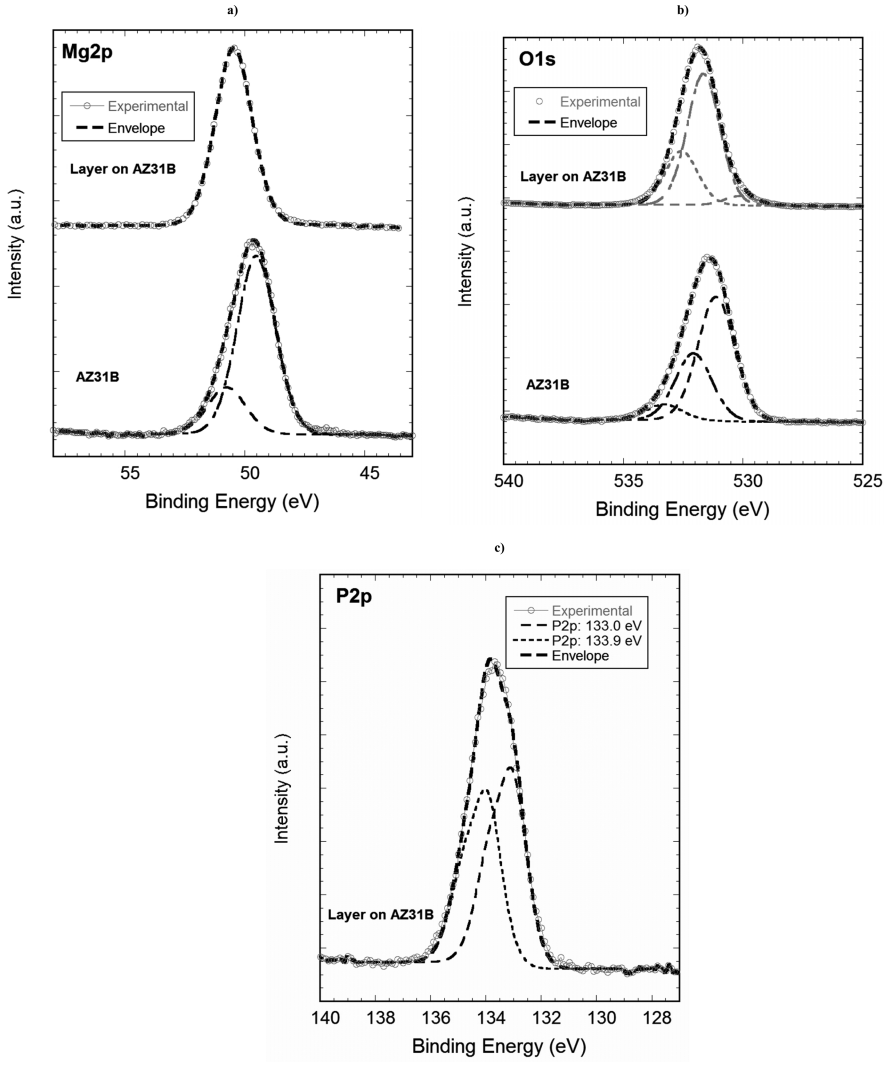

Figure 11. High-resolution XPS spectra, after background subtraction and curve fitting, for the pure AZ31B and for the coating layer generated in [EMIM][$EtPO_3H$] after chronoamperometry: (a) Mg 2p, (b) O 1s, and (c) P 2p.

magnesium hydroxides, magnesium carbonate, and magnesium phosphate together with aluminum phosphate.

The ARXPS data indicate the presence of some organic layer in the outer part of the film (Figure S6b, Supporting Information). The aluminum and phosphorus signals appear to be related.

The XPS analysis inside the wear tracks after the tribological tests was extremely difficult because of the insulating nature of this sample and due to the presence of a very rough surface. The beam size was set at 50 μm to detect the signal only from the wear scar excluding the contributions from the debris and from the noncontact area. The survey spectra showed the presence of C, O, Mg and barely detectable amounts of P, Al, and Zn. However, the data are not described here due to the asymmetry of the peaks caused by charging problems.

The present work presents the results obtained for just one ionic liquid. New possibilities should be explored by changing cation substituents and anion composition. In view of the oxidation from phosphonate to phosphate, it is proposed that ionic liquids containing phosphate anions should be studied.

4. CONCLUSIONS

The formation of a coating layer on magnesium alloy AZ31B from the 1-ethyl-3-methylimidazolium ethylphosphonate ionic liquid electrolyte by chronoamperometry has been described according to a 3D progressive mechanism. After the electrochemical treatment, no changes in the binding energies of the imidazolium cation are observed, while new P 2p and O 1s peaks are found at the ionic liquid surface, which could be due to the reaction of the phosphonate anion with the magnesium alloy. The surface coating layer grown on AZ31B from 1-ethyl-3-methylimidazolium ethylphosphonate is mainly composed of magnesium oxide, hydroxide, and carbonate, and magnesium and aluminum phosphate. The aluminum percentage is higher in the coating layer than in the base alloy, thus showing the relevance of alloy composition on the final results. The coating layer produces a maximum friction reduction of a 32% and wear reduction of a 90%, with respect to the unprotected alloy. Friction reductions are only observed after a running-in period of approximately 1 m of reciprocating sliding distance against steel. The enhancement of the tribological performance of AZ31B due to the reduction of wear debris can be attributed to the good adherence of the phosphate layer.

DOI: 10.1021/acsami.5b01167
ACS Appl. Mater. Interfaces 2015, 7, 10337−10347

■ ASSOCIATED CONTENT

Supporting Information

The Supporting Information showing IL geometry by Molecular Mechanics, chronoamperometry data, SEM-EDX of the uncoated alloy, and ARXPS data is available free of charge on the ACS Publications website at DOI: 10.1021/acsami.5b01167.

■ AUTHOR INFORMATION

Corresponding Author

*E-mail: mdolores.bermudez@upct.es.

Notes

The authors declare no competing financial interest.

■ ACKNOWLEDGMENTS

The authors wish to express their deep gratitude to Prof. N. D. Spencer (Laboratory for Surface Science and Technology. ETH Zürich, Switzerland) and to Dr. A. G. Bittermann (Electron Microscopy Center, EMEZ. ETH Zürich, Switzerland) for the facilities given to A.E.J. during her stay at the ETH Zürich. Mr. Cossu is acknowledged for the technical maintenance of the Thetaprobe. The authors are grateful to the laboratory of the Institute for Building Materials for the access to the electrochemical apparatus. This work received the financial support of the Ministerio de Economía y Competitividad (MINECO, Spain; MAT2011-23162 and MAT2014-55384-P). A.E.J. and T.E. are grateful to Ministerio de Educación (MECD, Spain) for grants JC2011-0074 and AP2010-3485, respectively.

■ REFERENCES

(1) Hornberger, H.; Virtanen, S.; Bocarini, A. R. Biomedical Coatings on Magnesium Alloys. A Review. *Acta Biomaterialia B* **2012**, 2442–2455.

(2) Wu, G.; Ibrahim, J. M.; Chu, P. K. Surface Design of Biodegradable Magnesium Alloys. A Review. *Surf. Coat. Technol.* **2013**, *233*, 2–12.

(3) Blau, P. J.; Walukas, M. Sliding Friction and Wear of Magnesium Alloy AZ91D Produced by Two Different Methods. *Tribol. Int.* **2000**, *33*, 573–579.

(4) An, J.; Li, R. G.; Lu, Y.; Chen, C. M.; Xu, Y.; Chen, X.; Wang, L. M. Dry Sliding Wear Behavior of Magnesium Alloys. *Wear* **2008**, *265*, 97–104.

(5) Taltavull, C.; Lopez, A. J.; Torres, B.; Rams, J. Dry Sliding Wear Behaviour of Laser Surface Melting Treated AM60B Magnesium Alloy. *Surf. Coat. Technol.* **2013**, *236*, 368–379.

(6) Song, G. L., Ed. *Corrosion of Magnesium Alloys*. Woodhouse: Cambridge (U.K.), 2011.

(7) Minami, I. Ionic Liquids in Tribology. *Molecules* **2009**, *14*, 2286–2305.

(8) Zhou, F.; Liang, Y.; Liu, W. Ionic Liquid Lubricants: Designed Chemistry for Engineering Applications. *Chem. Soc. Rev.* **2009**, *38*, 2590–2599.

(9) Bermúdez, M. D.; Jiménez, A. E.; Sanes, J.; Carrión, F. J. Ionic Liquids as Advanced Lubricant Fluids. *Molecules* **2009**, *14*, 2888–2908.

(10) Torimoto, T.; Tsuda, T.; Okazaki, K.; Kuwabata, S. New Frontiers in Materials Science Opened by Ionic Liquids. *Adv. Mater.* **2010**, *22*, 1196–1221.

(11) Palacio, M.; Bhushan, B. A Review of Ionic Liquids for Green Molecular Lubrication in Nanotechnology. *Tribol. Lett.* **2010**, *40*, 247–268.

(12) Schluecker, E.; Wasserscheid, P. Ionic Liquids in Mechanical Engineering. *Chem. Ing. Technol.* **2011**, *83*, 1476–1484.

(13) Somers, A.; Howlett, P.; MacFarlane, D. R.; Forsyth, M. A Review of Ionic Liquid Lubricants. *Lubricants* **2013**, *1*, 3–21.

(14) Angell, C. A.; Ansari, Y.; Zhao, Z. F. Ionic Liquids: Past, Present, and Future. *Faraday Discuss.* **2012**, *154*, 9–27.

(15) Special Issue: Ionic Liquids in Tribology. *Tribol. Lett.* **2010**, *40*, 213–284.

(16) Special Issue: Ionic Liquids as Lubricants. *Proc. Inst. Mech. Eng., Part J* **2012**, *226*, 889–1006.

(17) Predel, T.; Pohrer, B.; Schluecker, E. Ionic Liquids as Alternative Lubricants for Special Applications. *Chem. Eng. Technol.* **2010**, *33*, 132–136.

(18) Espinosa, T.; Jiménez, M.; Sanes, J.; Jiménez, A. E.; Iglesias, M.; Bermúdez, M. D. Ultralow Friction with a Protic Ionic Liquid Boundary Film at the Water-Lubricated Sapphire–Stainless Steel Interface. *Tribol. Lett.* **2014**, *53*, 1–9.

(19) Bermúdez, M. D.; Jiménez, A. E. Surface Interactions in Lubrication of Titanium, Aluminum, and Titanium-Aluminum Alloys with the Ionic Liquid $[C_2mim]Tf_2N$ under Increasing Temperature. *Proc. Inst. Mech. Eng., Part J* **2012**, *226*, 977–990.

(20) Jiménez, A. E.; Bermúdez, M. D. Ionic Liquids as Lubricants of Titanium–Steel Contact. Part 3. Ti_6Al_4V Lubricated with Imidazolium Ionic Liquids with Different Alkyl Chain Lengths. *Tribol. Lett.* **2010**, *40*, 237–246.

(21) Jiménez, A. E.; Bermúdez, M. D. Ionic Liquids as Lubricants of Titanium-Steel Contact. Part 2: Friction, Wear, and Surface Interactions at High Temperature. *Tribol. Lett.* **2010**, *37*, 431–443.

(22) Jiménez, A. E.; Bermúdez, M. D. Ionic Liquids as Lubricants of Titanium-Steel Contact. *Tribol. Lett.* **2009**, *33*, 111–126.

(23) Somers, A. E.; Khemchandani, B.; Howlett, P. C.; Sun, J. Z.; MacFarlane, D. R.; Forsyth, M. Ionic Liquids as Antiwear Additives in Base Oils: Influence of Structure on Miscibility and Antiwear Performance for Steel on Aluminum. *ACS Appl. Mater. Interfaces* **2013**, *5*, 11544–11553.

(24) Somers, A. E.; Biddulph, S. M.; Howlett, P. C.; Sun, J. Z.; MacFarlane, D. R.; Forsyth, M. A Comparison of Phosphorus and Fluorine Containing IL Lubricants for Steel on Aluminium. *Phys. Chem. Chem. Phys.* **2012**, *14*, 8224–8231.

(25) Qiao, D.; Wang, H. Z.; Feng, D. P. Tribological Performance of Phosphate Ionic Liquids as Lubricants for Steel-on-Aluminum Contacts. *Proc. Inst. Mech. Eng., Part J* **2013**, *227*, 1261–1271.

(26) Jiang, D.; Hu, L. T.; Feng, D. P. Tribological Behaviours of Novel Crown-Type Phosphate Ionic Liquids as Lubricants for Steel/Aluminium Contacts. *Ind. Lubr. Tribol.* **2013**, *65*, 219–225.

(27) Qiao, D.; Wang, H.; Feng, D. Tribological Performance and Mechanism of Phosphate Ionic Liquids as Additives in Three Base Oils for Steel-on-Aluminum Contact. *Tribol. Lett.* **2014**, *55*, 517–531.

(28) Espejo, C.; Carrión, F. J.; Bermúdez, M. D. Scratch Resistance of New Polystyrene Nanocomposites with Ionic Liquid-Modified Multi-Walled Carbon Nanotubes. *Tribol. Lett.* **2013**, *52*, 271–285.

(29) Saurín, N.; Sanes, J.; Bermúdez, M. D. Effect of Graphene and Ionic Liquid Additives on the Tribological Performance of Epoxy Resin. *Tribol. Lett.* **2014**, *56*, 133–142.

(30) Galinski, M.; Lewandowski, A.; Stepniak, I. Ionic Liquid as Electrolytes. *Electrochim. Acta* **2006**, *51*, 5567–5580.

(31) Zhang, S. J.; Sun, J.; Zhang, X. C.; Xin, J. Y.; Miao, Q. Q.; Wang, J. J. Ionic Liquid-based Green Processes for Energy Production. *Chem. Soc. Rev.* **2014**, *43*, 7838–7869.

(32) Ashassi-Sorkhabi, H.; Es'haghi, M. Corrosion Inhibition of Mild Steel in Acidic Media by [BMIm]Br Ionic Liquid. *Mater. Chem. Phys.* **2009**, *114*, 267–271.

(33) Zhang, Q. B.; Hua, Y. X. Corrosion Inhibition of Mild Steel by Alkylimidazolium Ionic Liquids in Hydrochloric Acid. *Electrochim. Acta* **2009**, *54*, 1881–1887.

(34) Shukla, S. K.; Murulana, L. C.; Ebenso, E. E. Inhibitive Effect of Imidazolium Based Aprotic Ionic Liquids on Mild Steel Corrosion in Hydrochloric Acid Medium. *Int. J. Electrochem. Sci.* **2011**, *6*, 4286–4295.

(35) Ibrahim, M. A. M.; Messali, M.; Moussa, Z.; Alzahrani, A. Y.; Alamry, B.; Hammouti, S. N. Corrosion Inhibition of Carbon Steel by Imidazolium and Pyridinium Cations Ionic Liquids in Acidic Environment. Port. *Electrochim. Acta* **2011**, *29*, 375–389.

DOI: 10.1021/acsami.5b01167
ACS Appl. Mater. Interfaces 2015, 7, 10337–10347

(36) Zarrouk, A.; Messali, M.; Zarrok, H.; Salghi, R.; Ali, A. A.; Hammouti, B.; Al-Deyab, S. S.; Bentiss, F. Synthesis, Characterization and Comparative Study of New Functionalized Imidazolium-based Ionic Liquids Derivatives Towards Corrosion of C38 Steel in Molar Hydrochloric Acid. *Int. J. Electrochem. Sci.* **2012**, *7*, 6998−7015.
(37) Likhanova, N. V.; Domínguez-Aguilar, M. A.; Olivares-Xometl, O.; Nava-Entzana, N.; Arce, E.; Dorantes, H. The Effect of Ionic Liquids with Imidazolium and Pyridinium Cations on the Corrosion Inhibition of Mild Steel in Acidic Environment. *Corros. Sci.* **2010**, *52*, 2088−2097.
(38) Guzmán-Lucero, D.; Olivares-Xometl, O.; Martínez-Palou, R.; Likhanova, N. V.; Domínguez-Aguilar, M. A.; Garibay-Febles, V. Synthesis of Selected Vinylimidazolium Ionic Liquids and Their Effectiveness as Corrosion Inhibitors for Carbon Steel in Aqueous Sulfuric Acid. *Ind. Eng. Chem. Res.* **2011**, *50*, 7129−7140.
(39) Likhanova, N. V.; Olivares-Xometl, O.; Guzmán-Lucero, D.; Domínguez-Aguilar, M. A.; Nava, N.; Corrales-Luna, M.; Mendoza, M. C. Corrosion Inhibition of Carbon Steel in Acidic Environment by Imidazolium Ionic Liquids Containing Vinyl-hexafluorophosphate as Anion. *Int. J. Electrochem. Sci.* **2011**, *6*, 4514−4536.
(40) Tüken, T.; Demir, F.; Kicir, N.; Sigircik, G.; Erbil, M. Inhibition Effect of 1-Ethyl-3-methylimidazolium Dicyanamide Against Steel Corrosion. *Corros. Sci.* **2012**, *59*, 110−118.
(41) Barham, H. A.; Brahim, S. A.; Rozita, Y.; Mohamed, K. A. Carbon Steel Corrosion Behaviour in Aqueous Carbonated Solution of MEA/[bmim] [DCA]. *Int. J. Electrochem. Sci.* **2011**, *6*, 181−198.
(42) Zhou, X.; Yang, H.; Wang, F. [BMIM]BF_4 Ionic Liquids as Effective Inhibitor for Carbon Steel in Alkaline Chloride Solution. *Electrochim. Acta* **2011**, *56*, 4268−4275.
(43) Scendo, M.; Uznanska J. The Effect of Ionic Liquids on the Corrosion Inhibition of Copper in Acidic Chloride Solutions. *Int. J. Corros.* **2011**, Art ID 718626.
(44) Abbott, A. P.; McKenzie, K. J. Application of Ionic Liquids to the Electrodeposition of Metals. *Phys. Chem. Chem. Phys.* **2006**, *8*, 4265−4279.
(45) Endres, F.; MacFarlane, D. R.; Abbott, A., Eds. *Electrodeposition from Ionic Liquids*. Wiley-VCH Verlag GmbH: Weinheim, Germany, 2008.
(46) Abbott, A. P.; Frisch, G.; Ryder, K. S. Electroplating Using Ionic Liquids. *Annu. Rev. Mater. Res.* **2013**, *43*, 335−358.
(47) Demadis, K. D.; Raptis, R. G.; Baran, P. Chemistry of Organophosphonate Scale Growth Inhibitors: 2. Structural Aspects of 2-Phosphonobutane-1,2,4-tricarboxylic Acid Monohydrate (PBTC·H_2O). *Bioinorg. Chem. Appl.* **2005**, *3*, 119−134.
(48) Khramov, A. N.; Balbyshev, V. N.; Kasten, L. S.; Mantz, R. A. Sol−Gel Coatings with Phosphonate Functionalities for Surface Modification of Magnesium Alloys. *Thin Solid Films* **2006**, *514*, 174−181.
(49) Grubac, Z.; Metikos-Hukovic, M.; Roncevic, I. S.; Petravic, M.; Peter, R. Functionalization of Biodegradable Magnesium Alloy Implants with Alkylphosphonate Self-Assembled Films. *Mater. Sci. Eng., C* **2013**, *33*, 2152−2158.
(50) Hoque, E.; DeRose, J. A.; Hoffmann, P.; Mathieu, H. J.; Bhushan, B.; Cichomski, M. Phosphonate Self-Assembled Monolayers on Aluminium Surfaces. *J. Chem. Phys.* **2006**, 124, Art. No. 174710.
(51) Ishizaki, T.; Okido, M.; Masuda, Y.; Saito, N.; Sakamoto, M. Corrosion Resistant Performance of Alkanoic and Phosphonic acids Derived Self-Assembled Monolayers on Magnesium Alloy AZ31 by Vapour-Phase Method. *Langmuir* **2011**, *27*, 6009−6017.
(52) Szillies, S.; Thissen, P.; Tabatabai, D.; Feil, F.; Fürbeth, W.; Fink, N.; Grundmeier, G. Formation and Stability of Organic Acid Monolayers on Magnesium Alloy AZ31: The Role of Alkyl Chain Length and Head Group Chemistry. *Appl. Surf. Sci.* **2013**, *283*, 339−347.
(53) Lathan, J. A.; Howlett, P. C.; Macfarlane, D. R.; Forsyth, M. Passive Film Formation in Dilute Ionic Liquid Solutions on Magnesium Alloy AZ31. *Electrochem. Commun.* **2012**, *19*, 90−92.
(54) Forsyth, M.; Howlett, P. C.; Tan, S. K.; MacFarlane, D. R.; Birbilis, N. An Ionic Liquid Surface Treatment for Corrosion Protection of Magnesium Alloy AZ31. *Electrochem. Solid-State Lett.* **2006**, *9*, B52−B55.
(55) Birbilis, N.; Howlett, P. C.; MacFarlane, D. R.; Forsyth, M. Exploring Corrosion Protection of Mg Via Ionic Liquid Pretreatment. *Surf. Coat. Technol.* **2007**, *201*, 4496−4504.
(56) Howlett, P. C.; Zhang, S.; MacFarlane, D. R.; Forsyth, M. An Investigation of a Phosphinate-based Ionic Liquid for Corrosion Protection of Magnesium Alloy AZ31. *Aus. J. Chem.* **2007**, *60*, 43−46.
(57) Howlett, P. C.; Efthimiadis, J.; Hale, P.; van Riessen, G. A.; MacFarlane, D. R.; Forsyth, M. Characterization of the Magnesium Alloy AZ31 Surface in the Ionic Liquid Trihexyl(tetradecyl)-phosphonium Bis(trifluoromethanesulfonyl)amide. *J. Electrochem. Soc.* **2010**, *157*, C392−C398.
(58) Howlett, P. C.; Khoo, T.; Mooketsi, G.; Efthimiadis, J.; MacFarlane, D. R.; Forsyth, M. The Effect of Potential Bias on the Formation of Ionic Liquid Generated Surface Films on Mg Alloys. *Electrochim. Acta* **2010**, *55*, 2377−2383.
(59) Sun, J.; Howlett, P. C.; MacFarlane, D. R.; Lin, J.; Forsyth, M. Synthesis and Physical Property Characterisation of Phosphonium Ionic Liquids Based on P(O)2(OR)2− and P(O)2(R)2− Anions with Potential Application for Corrosion Mitigation of Magnesium Alloys. *Electrochim. Acta* **2008**, *54*, 254−260.
(60) Efthimiadis, J.; Neil, W. C.; Bunter, A.; Howlett, P. C.; Hinton, B. R. W.; MacFarlane, D. R.; Forsyth, M. Potentiostatic Control of Ionic Liquid Surface Film Formation on ZE41 Magnesium Alloy. *ACS Appl. Mater. Interfaces* **2010**, *2*, 1317−1323.
(61) Forsyth, M.; Neil, W. C.; Howlett, P. C.; MacFarlane, D. R.; Hinton, B. R. W.; Rocher, N.; Kemp, T. F.; Smith, M. E. New Insights into the Fundamental Chemical Nature of Ionic Liquid Film Formation on Magnesium Alloy Surfaces. *ACS Appl. Mater. Interfaces* **2009**, *1*, 1045−1052.
(62) Howlett, P. C.; Efthimiadis, J.; Hale, P.; van Riesen, G. A.; MacFarlane, D. R.; Forsyth, M. Characterization of the Magnesium AZ31 Surface in the Ionic Liquid Trihexyl(tetradecyl) Phosphonium Bis(trifluoromethanesulfonyl)amide. *J. Electrochem. Soc.* **2010**, *157*, C392−C398.
(63) Forsyth, M.; Neil, W. C.; Wayne, C.; MacFarlane, D. R.; Hinton, B. R. W.; Rocher, N.; Kemp, T. F.; Smith, M. E. New Insights into the Fundamental Chemical Nature of Ionic Liquid Film Formation on Magnesium Alloy Surfaces. *ACS Appl. Mater. Interfaces* **2009**, *1*, 1045−1052.
(64) Huang, P. P.; Latham, J. A.; MacFarlane, D. R.; Howlett, P. C.; Forsyth, M. A Review of Ionic Liquid Surface Film Formation on Mg and its Alloys for Improved Corrosion Performance. *Electrochim. Acta* **2013**, *110*, 501−510.
(65) Elsentriecy, H. H.; Luo, H. M.; Meyer, H. M.; Grado, L. L.; Qu, J. Effects of Pre-Treatment and Process Temperature of a Conversion Coating Produced by an Aprotic Ammonium−Phosphate Ionic Liquid on Magnesium Corrosion Protection. *Electrochim. Acta* **2014**, *123*, 58−65.
(66) Pitawala, J.; Scheers, J.; Jacobson, P.; Matic, A. Physical Properties, Ion−Ion Interactions and Conformational States of Ionic Liquids with Alkylphosphonate Anions. *J. Phys. Chem. B* **2013**, *1178*, 8172−8179.
(67) Espinosa, T.; Sanes, J.; Jiménez, A. E.; Bermúdez, M. D. Surface Interactions, Corrosion Processes and Lubricating Performance of Protic and Aprotic Ionic Liquids with OFHC Copper. *Appl. Surf. Sci.* **2013**, *273*, 578−597.
(68) Espinosa, T.; Jiménez, A. E.; Martínez-Nicolás, G.; Sanes, J.; Bermúdez, M. D. Abrasion Resistance of Magnesium Alloys with Surface Films Generated from Phosphonate Imidazolium Ionic Liquids. *Appl. Surf. Sci.* **2014**, *320*, 267−273.
(69) Espinosa, T.; Sanes, J.; Bermúdez, M. D. Halogen-free Phosphonate Ionic Liquids as Precursors of Abrasion Resistant Surface Layers on AZ31B Magnesium Alloy. *Coatings* **2015**, *5*, 39−53.
(70) Smith, E. F.; Rutten, F. J. M.; Villar-García, I. J.; D. Briggs, D.; Licence, P. Ionic Liquids in Vacuo: Analysis of Liquid Surfaces using Ultra-high Vacuum Techniques. *Langmuir* **2006**, *22*, 9386−9392.

DOI: 10.1021/acsami.5b01167
ACS Appl. Mater. Interfaces 2015, 7, 10337−10347

(71) Arcifa, A.; Rossi, A.; Espinosa-Marzal, R. M.; Spencer, N. D. Environmental Influence on the Surface Chemistry of Ionic-Liquid-Mediated Lubrication in a Silica/Silicon Tribopair. *J. Phys. Chem. C* **2014**, *118*, 29389−29400.
(72) Thirsk, H. R.; Harrison, J. A. *A Guide to the Study of Electrode Kinetics*; Academia Press: London, 1972.
(73) Bade, K.; Tsakova, V.; Schultze, J. W. Nucleation, Growth and Branching of Polyaniline from Microelectrode Experiments. *Electrochim. Acta* **1992**, *37*, 2255−2261.
(74) Zhang, J. F.; Yan, C. W.; Wang, F. H. Electrodeposition of Al-Mn alloy on AZ31B magnesium alloy in molten salts. *Appl. Surf. Sci.* **2009**, *255*, 4926−4932.
(75) Crobu, M.; Rossi, A.; Mangolini, F.; Spencer, N. D. Chain-Length-Identification Strategy in Zinc Polyphosphate Glasses by Means of XPS and ToF-SIMS. *Anal. Bioanal. Chem.* **2012**, *403*, 1415−1432.
(76) NIST X-ray Photoelectron Spectroscopy Databasehttp://srdata.nist.gov/xps/ (last accessed 03/31/2015).
(77) Cumpson, P. J. Angle-Resolved XPS and AES: Depth Resolution Limits and a General Comparison of Properties of Depth-Profile Reconstruction Methods. *J. Electron Spectrosc. Relat. Phenom.* **1995**, *73*, 25−52.
(78) Lovelock, K. R. J.; Villar-García, I. J.; Maier, F.; Steinrück, H. P.; Licence, P. Photoelectron Spectroscopy of Ionic Liquid-based Interfaces. *Chem. Rev.* **2010**, *110*, 5158−5190.
(79) Feliú, S.; Merino, M. C.; Arrabal, R.; Coy, A. E.; Matykina, E. XPS Study of the Effect of Aluminium on the Atmospheric Corrosion of the AZ31 Magnesium Alloy. *Surf. Interface Anal.* **2009**, *41*, 143−150.

DOI: 10.1021/acsami.5b01167
ACS Appl. Mater. Interfaces 2015, 7, 10337−10347